RESEARCH ARTICLE

Check for updates

Sn-doped mixed-halide Li₆PS₅Cl₀.₅Br₀.₅ argyrodite with enhanced chemical stability for all-solid-state batteries†

$Sn-doped\ mixed-halide\ Li_6PS_5Cl_{0.5}Br_{0.5}\ argyrodite\ with\ enhanced\ chemical\ stability\ for\ all-solid-state\ batteries$†

Yoonjae Cho, [ID] [a] Jung Hwan Song, [ID] [a] Ji Eun Wang, [ID] [b] Do Kyung Kim [ID] ★[ac] and Dong Jun Kim [ID] ★[b]

The synthesis and characterization of Sn-doped $Li_6PS_5Cl_{0.5}Br_{0.5}$ solid-state electrolytes are presented. By incorporating Cl and Br, the solubility of Sn dopants in the argyrodite framework is significantly improved without compromising the high ionic conductivity of material. Sn substitution for P enhances both the chemical robustness and interfacial stability of the electrolyte, addressing key challenges in electrolyte stability. The inclusion of Sn strengthens the structural integrity of $Li_6PS_5Cl_{0.5}Br_{0.5}$, mitigating atmospheric degradation. Electrochemical studies reveal that Sn doping markedly increases ionic conductivity and reduces the activation energy for Li-ion mobility, thereby improving battery performance. Structural analyses indicate that Sn incorporation expands the unit cell and facilitates the formation of a Li–Sn alloy at the electrolyte–electrode interface. This alloy formation promotes rapid Li-ion migration and stabilizes the interface, contributing to enhanced electrochemical stability. The findings underscore the synergistic benefits of halogen substitution and Sn doping, demonstrating their collective impact on the performance and durability of sulfide-based solid electrolytes.

1. Introduction

In the quest to mitigate the environmental footprint of energy consumption, the shift from fossil fuels to more sustainable energy sources has led to significant interest in advanced energy storage technologies. Among these, secondary batteries are pivotal components in the transition towards a greener energy landscape.[1] Lithium-ion batteries (LIBs), with their high energy and power densities, have emerged as the frontrunners in this domain, finding widespread applications in portable electronics, electric vehicles, and energy storage systems.[1–3] Although conventional LIBs have made significant progress, they still struggle with inherent limitations, such as safety risks posed by flammable organic solvent-based electrolytes.[3–5]

The pursuit of safer and more efficient energy storage solutions has spurred the development of all-solid-state batteries (ASSBs), which potentially address the shortcomings of

their LIB counterparts.[6–8] Moreover, the integration of lithium metal anodes into ASSBs promises significantly higher energy densities, owing to the low atomic weight and redox potential of Li elements.[7–12] Among the diverse candidates for solid-state electrolytes (SSEs), argyrodite structured sulfides, particularly those based on the Li_6PS_5X (X = Cl, Br, I) composition, have garnered attention. Their high ionic conductivity and cost-effective precursors position them as promising contenders.[13–16]

Despite the potential benefits, employing argyrodite compounds in SSEs faces substantial challenges. One major issue is the inherently narrow electrochemical stability window of these materials, which increases their susceptibility to decomposition upon interacting with electrodes.[17–22] This decomposition leads to the accumulation of insulating by-products at the anode interface, which, in turn, promotes the formation of problematic dendritic structures during the charge–discharge cycles.[11,19–23] Furthermore, the air sensitivity of sulfide electrolytes complicates their practical use. Exposure to atmospheric moisture triggers the release of toxic hydrogen sulfide gas from the sulfur components, posing safety hazards and deteriorating the electrolyte ionic conductivity.[24,25] To address these challenges, cation doping on the P site of argyrodite solid electrolytes was investigated.[26–31] Aliovalent doping has been considered a method for enhancing the ionic conductivity of Li_6PS_5X by introducing larger cations into the lattice structure,

[a] Department of Materials Science and Engineering, Korea Advanced Institute of Science and Technology (KAIST), 291 Daehak-ro, Yuseong-gu, Daejeon 34141, Republic of Korea. E-mail: dkkim@kaist.ac.kr

[b] School of Chemistry, The University of New South Wales, Sydney, NSW 2052, Australia. E-mail: dongjun.kim@unsw.edu.au

[c] School of Mechanical and Manufacturing Engineering, The University of New South Wales, High St, Kensington, NSW 2052, Australia

† Electronic supplementary information (ESI) available. See DOI: https://doi.org/10.1039/d5qm00394f

which expands the lattice parameters and improves ionic transport.[31–33] Recent studies have also shown that this approach can enhance interfacial stability by forming an interfacial layer that stabilizes lithium metal reactivity.[28–30] Among various dopants, Sn has drawn attention as an effective additive for improving the electrochemical stability and moisture resistance of sulfide solid electrolytes.[24,25,28–30] However, its large atomic radius poses a limitation for substitution in LPSCl argyrodite electrolytes, which exhibit high ionic conductivity but feature a small unit cell size due to the small Cl halide ion. Consequently, Sn doping has been achieved in LPSBr or LPSI, which have larger halide ions and unit cell sizes capable of accommodating larger cations, albeit with a trade-off of reduced ionic conductivity.[29,30]

In this study, we explored the strategic substitution of Sn for P within $Li_6PS_5Cl_{0.5}Br_{0.5}$ (LPSClBr) to enhance the ionic conductivity, interfacial stability, and air stability of ASSBs. The LPSClBr framework, with its larger unit cell compared to Li_6PS_5Cl, facilitates the substitution of Sn and optimized S^{2-}/X^- disorder and lattice softness. This structural adjustment results in high ionic conductivity, reaching the order of 10^{-3} S cm^{-1}. Crucially, the aliovalent substitution promotes the formation of a lithiophilic Li–Sn alloy at the electrolyte interface, stabilizing the interface during electrochemical cycling. Furthermore, the Sn substitution significantly improves air stability by forming stronger bonds with sulfur compared to phosphorus, thereby reducing oxygen reactivity and enhancing the stability of the PS_4^{3-} unit. Comprehensive full cell testing has demonstrated the improved electrochemical performance and stability attributable to Sn substitution, underscoring its significant impact on the functionality and safety of ASSBs. Collectively, this study proposes a strategy to overcome the doping and solubility limitations of aliovalent cations in argyrodite sulfide solid electrolytes, which exhibit high ionic conductivity, by carefully selecting and combining halide ions. Moreover, our findings underscore the benefits of partial Sn substitution in LPSClBr SSEs, establishing it as a promising approach for developing high-performance ASSBs.

2. Experimental

2.1. Materials preparation

$Li_{6+x}Sn_xP_{1-x}S_5Cl_{0.5}Br_{0.5}$ (x = 0, 0.025, 0.05, 0.075) sulfide solid electrolytes were fabricated in an inert argon atmosphere. For this purpose, 3 g of Li_2S, P_2S_5, $SnCl_2$, S, LiCl, and LiBr precursors, all sourced from Sigma Aldrich, were weighed and subjected to high-energy planetary ball milling (Pulverisette 5, Fritsch) at a speed of 300 rpm for 20 hours. The mixed powder was then compacted under a pressure of 200 MPa for one minute. The compaction was followed by an annealing step, carried out at 550 °C for 5 hours in an argon environment, with a temperature increasing rate of 5 °C min^{-1}.

2.2. Materials characterization

The synthesized $Li_{6+x}Sn_xP_{1-x}S_5Cl_{0.5}Br_{0.5}$ solid electrolytes were characterized using XRD, Raman spectra, and EDS analysis.

XRD was conducted in the Rigaku smart lab with Cu-Kα radiation (λ_1 = 1.54051 Å) operating at 45 kV and 200 mA. It was used to confirm the crystal phase of electrolytes. The measurement was performed in the 2θ range from 10° to 70°, with a scanning rate of 10° min^{-1} using an air-tight XRD sample holder. For XRD Rietveld refinement, the measurement was performed in the 2θ range from 10° to 120°, with a scanning rate of 2° min^{-1}. Raman spectrometer (Horiba Lab-Ram HR Evolution Visible_NIR) analysis was conducted with a laser of 514 nm. The measurement was performed in the wavenumber range from 200–600 cm^{-1}. The shape and atomic distribution of the solid electrolyte particle were confirmed by field-emission scanning electron microscopy (FE-SEM, Hitachi SU8230), and EDS (Oxford X-Max). Each sample was loaded into the SEM without being exposed to the air. In order to confirm the effect of Sn substitution on the electrochemical stability of the electrolyte against lithium metal anode, cycled lithium metal (after symmetric cell test) was characterized using X-ray photoelectron spectroscopy (XPS, Axis-Supra). XPS measurements were performed using a Kα with an automated monochromatic X-ray source emitting Al-Kα 1486.7 eV X-ray photons. The XPS data was calibrated using the binding energy of 284.6 eV for carbon 1s.

2.3. Electrochemical measurements

Solid electrolytes were evaluated with pressure cells (Premium Glass Co.). Ionic conductivity measurement was performed with SUS on both sides of the solid electrolyte at various temperatures (30 °C, 40 °C, 50 °C, 60 °C, 70 °C). It was conducted in a frequency range of 10 MHz to 1 Hz, with a voltage amplitude of 10 mV using an impedance/gain-phase analyzer (Solartron SI 1260). The cyclic voltammetry test was performed at −0.5 to 5 V (vs. Li/Li$^+$) voltage range and a scan rate of 10 mV s^{-1}. The symmetric cell test and galvanostatic charge–discharge performance were conducted by a Won-A-Tech battery cycler (WBCS 3000). The galvanostatic charge–discharge test was performed under 0.1C rate, with cut-off voltages at 3.0 and 4.3 V (vs. Li/Li$^+$) at a temperature of 30 °C. The charge–discharge test was initiated without any prior pre-cycling steps.

2.4. Air stability measurements

To evaluate enhanced air stability due to Sn substitution, the mass change of the electrolyte in the air atmosphere was measured using the TGA instrument (Mettler Toledo TGA2). Next, 150 mg of solid electrolyte was pressed into the pellet. 12 hours after pellets were exposed to the atmosphere of 30 °C and 7 RH%, ionic conductivity was measured.

2.5. Fabrication of all-solid-state batteries

For the cathode preparation, solid electrolyte, $LiCoO_2$ (L&F co.), and SuperP (TIMCAL) were mixed in a weight ratio of 79:20:1 using mortar and pestle. Subsequently, 120 mg of the synthesized solid electrolyte powder was introduced into a 10 mm diameter SUS mold and compacted at a pressure of 200 MPa. Subsequently, 12 mg of the cathode composite was evenly

spread on top of the electrolyte and compressed at a higher pressure of 300 MPa. The anode was lithium metal foil with a diameter of 10 mm and a thickness of 200 μm. In addition, symmetric cells were fabricated using lithium metal coupled with another lithium metal instead of a cathode composite.

3. Results and discussions

3.1. Structure characterization and ionic conductivity of $Li_{6+x}Sn_xP_{1-x}S_5Cl_{0.5}Br_{0.5}$

Ionic conductivity in lithium argyrodite compounds is primarily influenced by the type and distribution of halogen ions within the electrolyte framework. The substitution of Br^- and Cl^- ions, which have dimensions closely aligned with those of S^{2-} ions, introduces significant disorder into the lattice. This intrinsic disorder is a key factor in the high ionic conductivity, reaching values above 10^{-3} S cm^{-1}, as it disrupts the orderly lattice arrangement and creates more pathways for ion movement. In contrast, the larger size of I^- limits its effective integration into the lattice, thereby reducing the overall conductivity.[15,34]

In addition to ionic size, the softness of the lattice—determined by the polarizability of the halogen ions—plays a crucial role in facilitating ionic mobility.[15,35] As polarizability increases from Cl to Br to I, the reduction in electrostatic forces between lithium-ions and halogen ligands expands the lattice structure and creates more efficient diffusion pathways. This effect is particularly significant in mixed-halide systems such as LPSClBr, where the interplay between lattice disorder and softness contributes to exceptionally high ionic conductivity.[35,36] The synergy of these factors—ionic size similarity and lattice softness—establishes LPSClBr a highly effective material for solid-state electrolytes. Furthermore, expanding the unit cell size through Br incorporation enhances the doping capability.

The $Li_{6+x}Sn_xP_{1-x}S_5Cl_{0.5}Br_{0.5}$ electrolyte was synthesized using a solid-state synthesis method (Fig. 1(a)) with x values of 0 (LPSClBr), 0.025 (Sn2.5@Agy), 0.05 (Sn5@Agy), and 0.075 (Sn7.5@Agy). The precursors (Li_2S, P_2S_5, LiCl, LiBr, $SnCl_2$, and S) in the required stoichiometric ratio were homogeneously mixed through high-energy milling for 20 hours. Subsequently, heat treatment was conducted at 550 °C for 5 hours under Ar atmosphere.

X-ray diffraction (XRD) analysis results for the synthesized $Li_{6+x}Sn_xP_{1-x}S_5Cl_{0.5}Br_{0.5}$ (Fig. 1(b)–(d)) closely align with the reference phase of LPSClBr, indicating the successful synthesis of crystalline solid electrolyte with a high level of crystallinity and phase purity. The stability of this structure across varying dopant levels suggests that the introduction of dopants into the argyrodite phase is accomplished without compromising the inherent crystalline architecture. Notably, as demonstrated in Fig. 1(b) and (d), the main peaks indicative of the argyrodite structure undergo a subtle shift toward lower 2θ values as the Sn substitution increases. This phenomenon can be attributed to the substitution of P^{5+} ions, whose ionic radius of 38 pm, with Sn^{4+} ions, which possess a relatively larger ionic radius of 69 pm, leading to an expansion of the Li-argyrodite unit cell volume.[37] At the Sn substitution level of 7.5% (Sn7.5@Agy),

Fig. 1(c) and (d) illustrate the onset and incremental rise in impurity secondary phases such as Li_4SnS_4. These secondary phases indicate a critical limit to the tuning of the composition for maintaining its desired structural and electrochemical integrity.[26] Fig. S1 (ESI†) presents the Rietveld analysis results for LPSClBr and Sn5@Agy. Both electrolytes exhibited a cubic argyrodite phase ($F\bar{4}3m$ space group), with unit cell parameters detailed in Table S1 (ESI†). Upon Sn doping, the unit cell parameter increased from 9.90337 to 9.9195, indicating an expansion in the unit cell volume.

Raman spectroscopy was conducted to further investigate the structural changes induced by Sn substitution. The Raman spectra depicted in Fig. 1(e) cover a 200 to 600 cm^{-1} range. The band at 423 cm^{-1} confirms the presence of the PS_4^{3-} tetrahedral anion unit, a main component of the $Li_{6+x}Sn_xP_{1-x}S_5Cl_{0.5}Br_{0.5}$ phase.[38] As the Sn substitution increases, the PS_4^{3-} band shifts slightly to lower wavenumbers, suggesting that the bonds are extending due to the lattice expansion, consistent with the XRD results. A larger increase in Sn substitution introduces an additional, distinct band at 346 cm^{-1}, associated with the SnS_4^{4-} unit,[39] suggesting the emergence of hybrid $(P/Sn)S_4^{3-}$ units, indicative of Sn substituting for P sites. These findings also confirm that the structural integrity of the $(P/Sn)S_4^{3-}$ unit is retained after substitution.

The structural morphology and elemental distribution of electrolyte samples were investigated through energy-dispersive X-ray spectroscopy (EDS) coupled with SEM analysis (Fig. S2(a)–(d), ESI†). The EDS analysis focused on elements such as P, Sn, S, Cl, and Br and revealed a homogeneous distribution across the solid electrolyte particles. In the case of the Sn7.5@Agy electrolyte, however, an uneven Sn distribution was apparent with Sn-rich domains. The findings from XRD and Raman studies suggest that a Sn substitution level of 7.5% may exceed the material's doping capacity, resulting in phase separation and the formation of impurities such as Li_4SnS_4.

The ionic conductivity of solid electrolytes was measured using electrochemical impedance spectroscopy (EIS). For EIS measurements, pellets were prepared by compressing 100 mg of the electrolyte and placing stainless steel rods on each pellet side as blocking electrodes. Analysis was conducted at 30, 40, 50, 60, and 70 °C in a frequency range from 10 MHz to 1 Hz. The ionic conductivity (σ_{Li}) and activation energy (E_a) of Li-ion transport were calculated using the following equations,

$$\sigma_{Li} = \frac{l}{R \times A} \quad (1)$$

$$\sigma_{Li} = D \times \exp\left(\frac{-E_a}{K \times T}\right) (S\ cm^{-1}) \quad (2)$$

where R is the bulk resistance of the solid electrolyte, l is the thickness of the electrolyte pellet (cm), A is the area of the pellet (cm^2), D is the pre-exponential constant, K is the Boltzmann constant, and T is the temperature (K). Fig. 2(a) and (b) display the Nyquist and Arrhenius plots, respectively, derived from EIS measurements across the temperature range of 30 to 70 °C for each electrolyte sample.
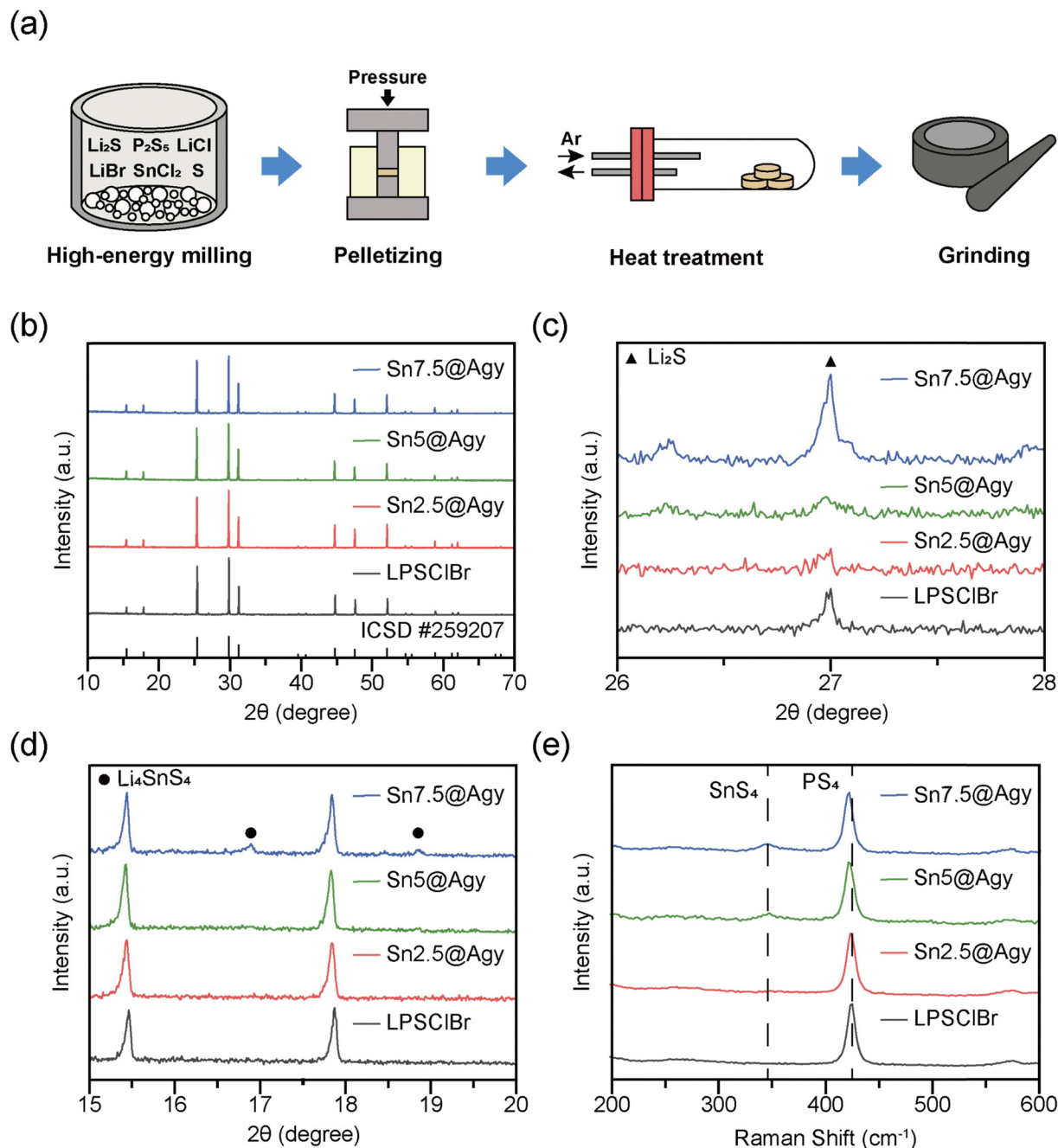
Fig. 1 (a) Synthesis process of $Li_{6+x}Sn_xP_{1-x}S_5Cl_{0.5}Br_{0.5}$ sulfide solid electrolyte. (b) XRD patterns of synthesized $Li_{6+x}Sn_xP_{1-x}S_5Cl_{0.5}Br_{0.5}$ electrolyte with respect to Sn substitution amount. (c) Magnified section of the XRD patterns ($26° < \theta < 28°$). (d) Magnified section of the XRD patterns ($15° < \theta < 20°$). (e) Raman spectra of the synthesized $Li_{6+x}Sn_xP_{1-x}S_5Cl_{0.5}Br_{0.5}$ electrolyte.

The ionic conductivity of LPSClBr was 1.81 mS cm^{-1} at room temperature similar to that reported for Li-argyrodite (10^{-2}–10^{-3} mS cm^{-1}).[13,19] As the Sn substitution concentration increases to 2.5% (Sn2.5@Agy) and 5% (Sn5@Agy), the ionic conductivity increases to 2.07 and 2.34 mS cm^{-1}, respectively. This increase can be attributed to an increase in the unit cell volume within the lattice due to Sn doping, which has a larger ionic radius compared to P, thereby increasing the volume of the lithium pathway channel. Additionally, by substituting at the P^{5+} site with an aliovalent element Sn^{4+} in a different

oxidation state, the concentration of lithium-ions increases through charge compensation.[31–33] This phenomenon can be explained using the defect equation in Kröger–Vink notation.

$$SnCl_2 + Li\ sources(Li_2S, LiCl, LiBr) + V'_{Li} \rightarrow Sn'_p + Li^x_{Li} \quad (3)$$

The substitution of P^{5+} with x moles of Sn^{4+} introduces x moles of lithium atoms to maintain charge balance, thereby increasing the lithium solubility within the crystal structure ($Li_6PS_5Cl_{0.5}Br_{0.5} \rightarrow Li_{6+x}Sn_xP_{1-x}S_5Cl_{0.5}Br_{0.5}$). On the other
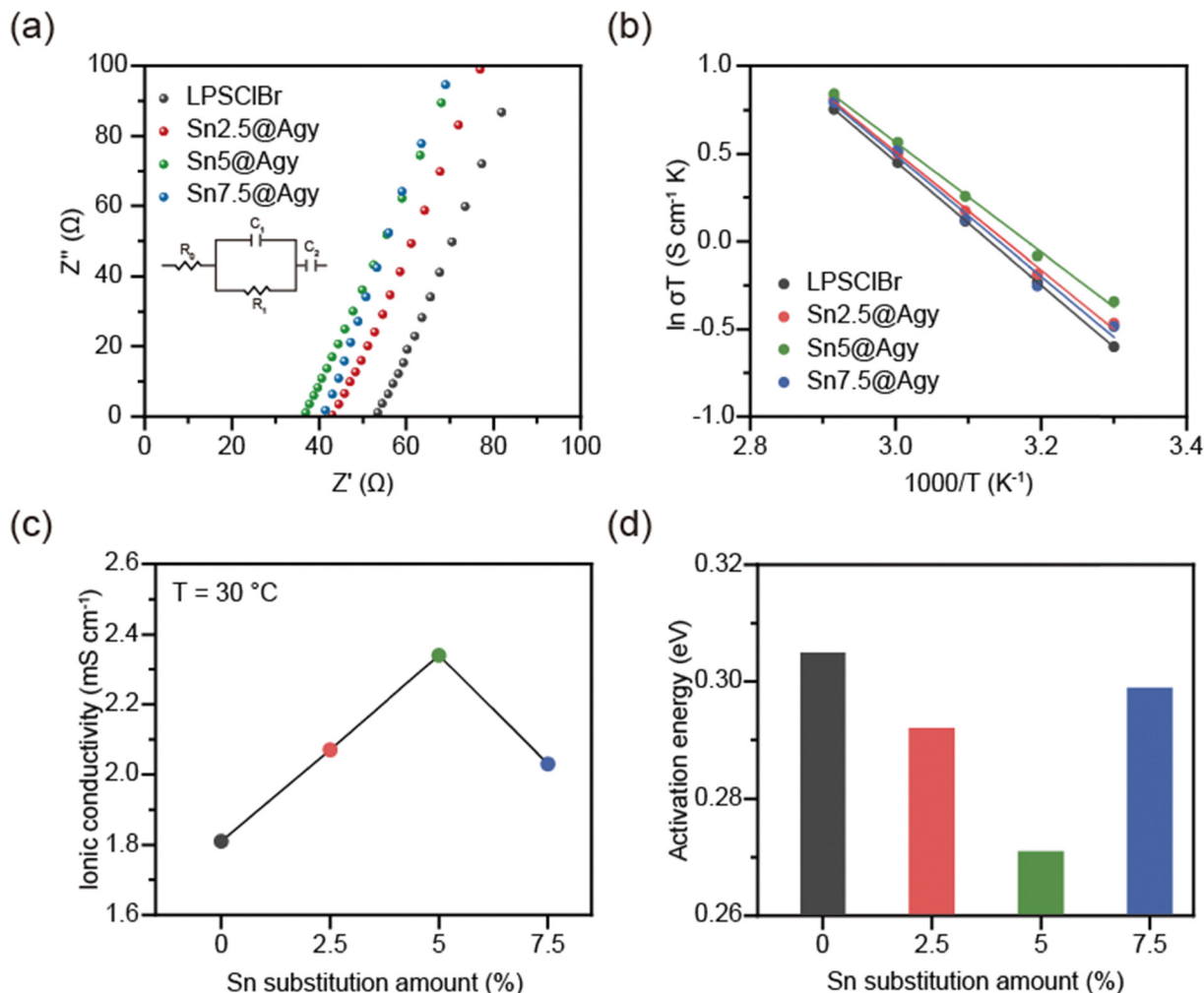
Fig. 2 (a) Nyquist plots of pelletized solid electrolytes at 30 °C. (b) Arrhenius plot of the pelletized solid electrolytes. (c) The ionic conductivity of solid electrolytes at 30 °C. (d) The activation energy of solid electrolytes against Sn substitution amount.

hand, the ionic conductivity of Sn7.5@Agy was lower than that of Sn5@Agy, a decrease attributed to the increased impurities, such as Li_4SnS_4, as indicated by XRD analysis.

The activation energy of lithium-ion transport was calculated using the Arrhenius equation according to the amount of Sn substitution, as shown in Fig. 2(d). As the Sn substitution increased from 0 to 2.5 and to 5%, the activation energy decreased to 0.305, 0.292, and 0.271 eV, respectively. However, in the Sn7.5@Agy electrolyte, the decreasing trend reversed, and the activation energy increased to 0.299 eV. Hence, the Sn5@Agy has the lowest activation energy, indicating the easiest Li^+ movement and explaining the highest ionic conductivity among the different substitution amounts. Therefore, subsequent electrochemical analyses were conducted using LPSClBr and Sn5@Agy, which exhibit the highest ionic conductivity and the lowest activation energy.

3.2. Electrochemical performance of synthesized $Li_{6+x}Sn_xP_{1-x}S_5Cl_{0.5}Br_{0.5}$

In order to assess the electrochemical stability window of the LPSClBr and Sn5@Agy solid electrolytes, cyclic voltammetry (CV) was conducted. Samples were prepared by compressing

120 mg of solid electrolytes into 10 mm diameter pellets. These were then sandwiched between a stainless steel and lithium foils, forming a $Li|Li_{6+x}Sn_xP_{1-x}S_5Cl_{0.5}Br_{0.5}|SUS$ cell configuration. The first and third CV cycles for LPSClBr and Sn5@Agy solid electrolytes are displayed in Fig. S3(a) and (b) (ESI†). Both electrolytes exhibited a single cathodic and anodic peak corresponding to lithium deposition ($Li^+ + e^- \rightarrow Li$) and dissolution ($Li \rightarrow Li^+ + e^-$), demonstrating the reversible lithium plating capability of the electrolyte. No additional redox peaks were observed, which underscores the wide electrochemical stability window of the electrolyte. This observation and its correlation with electrochemical stability will be further explored in subsequent discussions below.

Next, symmetric cells were fabricated, and cycling tests were conducted. The results, displayed in Fig. 3, were obtained at 30 °C using LPSClBr and Sn5@Agy electrolytes. For these symmetric cell tests, lithium metal was attached to both sides of an electrolyte pellet configured as Li|SSE|Li. Fig. 3(a) and (b) illustrate the progressive evaluation of critical current density, starting at 0.05 mA cm^{-2} and escalating by 0.05 mA cm^{-2} after every three cycles of lithium stripping and plating. The distinct
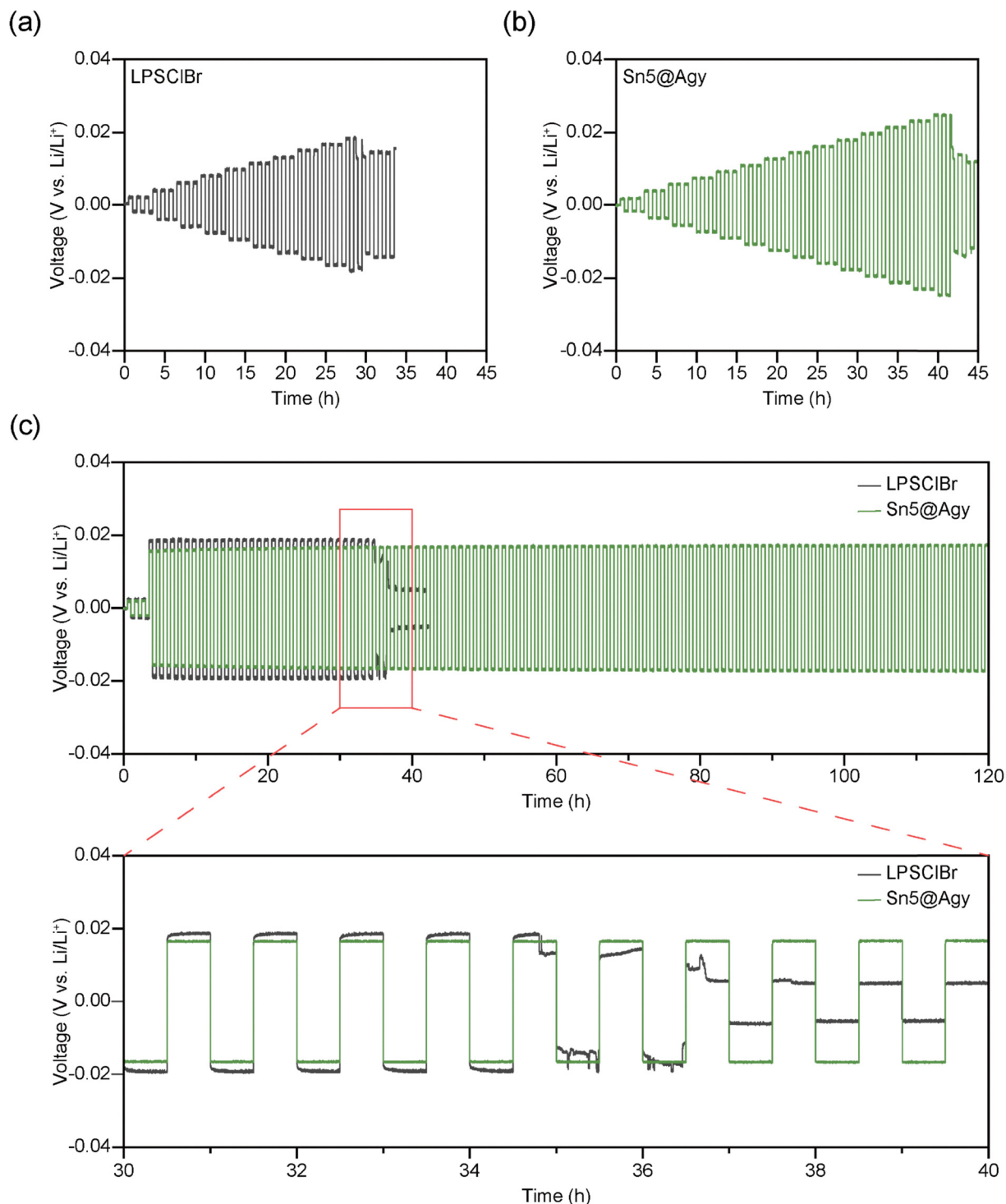
Fig. 3 Symmetric cell test: (a) critical current density of LPSClBr. (b) Critical current density of Sn5@Agy. (c) Symmetric cell test at constant current density (0.4 mA cm^{-2}) and a magnified section of the symmetric cell test (30–40 h).

performance differences between Sn-doped samples indicate that Sn substitution plays a crucial role in mitigating lithium dendrite formation. The LPSClBr electrolyte underwent a voltage drop when the current reached 0.45 mA cm^{-2}. In contrast, the Sn5@Agy electrolyte exhibited consistent stability, with no voltage drop observed even as the current density increased to 0.65 mA cm^{-2}, signifying a substantial increase in current density capacity.

A long-term lithium plating/stripping stability was performed at a constant current density of 0.4 mA cm^{-2} to evaluate the interface stability between the solid electrolyte and lithium metal further. Initial overpotential measurements, presented in

Fig. 3(c), indicate that Sn5@Agy exhibited an overpotential of 15.5 mV, lower than the 18.3 mV for LPSClBr. Notably, LPSClBr underwent a short circuit after just 34 hours, whereas Sn5@Agy demonstrated no short circuit over a prolonged period of 125 hours. A significant difference in the cycling results is possibly attributed to Sn substitution, which appears to modify the voltage profile during the test period. Specifically, from 30 to 35 hours into the symmetric cell testing, LPSClBr showed clear signs of polarization, characterized by arcs and plateaus. According to previous reports, these phenomena are likely due to dendrite formation, dead lithium, and interface by-products, all of which obstruct lithium-ion transport and contribute to polarization.[9,20,40] Conversely, the voltage profile for Sn5@Agy did not show any polarization, suggesting that the presence of Sn helps to form a stable interface that suppresses side reactions, enhances Li$^+$ diffusion, suppresses side reactions, and facilitates more rapid ion migration across the interface. Moreover, during symmetric cell tests at both critical and constant current densities, Sn5@Agy consistently showed a lower overpotential compared to LPSClBr. This observation confirms that Sn substitution not only improves ionic conductivity but also enhances the compatibility of the electrolyte with lithium metal. The increased ionic conductivity results in a more uniform distribution of current density across the lithium metal surface, which is instrumental in suppressing dendrite growth. These findings affirm that Sn substitution in LPSClBr markedly improves the electrochemical stability of Li metal in sulfide solid electrolytes XPS analysis of the Li metal interfaces with LPSClBr and Sn5@Agy electrolytes was conducted after the 20th cycle of the symmetric cell test (Fig. S4, ESI†) at a current density of 0.1 mA cm^{-2} to reveal the effect of Sn substitution on electrolyte-lithium metal interface compatibility. In Fig. 4(a) and (b), the S 2p spectra display binding energies at 161.10 eV (S 2p3/2) and 162.30 eV (S 2p1/2), corresponding to the Li-argyrodite PS$_4$$^{3-}$ tetrahedral anion.[41] At the interface, lithium metal reduces the sulfide solid electrolyte, leading to insulating by-products such as Li$_2$S and Li$_3$P, which contribute to an uneven SEI layer.[21,23] The reduced formation of Li$_2$S in the Sn5@Agy electrolytes emphasizes the effectiveness of Sn doping in minimizing electrolyte decomposition. Moreover, with Sn5@Agy, the reduced sulfite with a binding energy of 167.1 eV at the interface indicates that Sn substitution may mitigate reactions with atmospheric oxygen in the environment.[42] The beneficial impact of Sn substitution could stem from the higher bond dissociation energy of Sn–S at 464 kJ mol^{-1} compared to 346 kJ mol^{-1} for P–S bonds, suggesting stronger Sn–S bonding that enhances the structural integrity of the Li argyrodite electrolyte, and less decomposition at the interface with the Li metal anode.[43] The XPS Sn 3d spectra also highlight the formation of a Li–Sn alloy, which is beneficial for enhancing interfacial stability. The detection of Li–Sn alloy and Sn^{x+} species at binding energies of 484.22 and 485.4 eV suggests that this alloy acts as a passivation layer at the interface.[44] This alloy has reportedly enhanced Li$^+$ ion diffusion, facilitating rapid ion migration at the interface.[45] Moreover, the lithiophilic nature of the Li–Sn alloy reduces the energy barriers for

lithium nucleation and promotes homogeneous lithium deposition by creating multiple nucleation sites, thereby inhibiting dendrite formation through uniform lithium plating, as evidenced by our electrochemical cycling data.[46] The existence of these interfacial species is additionally supported by the Li 1s spectra in Fig. S5 (ESI†).

3.3. Air stability of Li$_{6+x}$Sn$_x$P$_{1-x}$S$_5$Cl$_{0.5}$Br$_{0.5}$

Sulfide solid electrolytes such as Li-argyrodite suffer from poor air stability due to the high reactivity of sulfur. Upon exposure to moisture, LPSClBr undergoes substitution of sulfur by oxygen, resulting in the formation of impurities such as LiCl, Li$_2$S, Li$_3$PO$_4$, and H$_2$S, which lead to a significant degradation in ionic conductivity:[25]

$$Li_6PS_5X \ (X = Cl, Br, I) \ (s) + 4H_2O \ (g) \rightarrow LiX \ (s) \\ + Li_2S \ (s) + Li_3PO_4 \ (s) + 4H_2S \ (g) \quad (4)$$
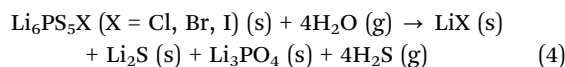
This phenomenon occurs even at low moisture levels, necessitating strict regulation of oxygen and moisture levels to below 1 ppm. Therefore, improving their air stability is crucial for the viable commercialization of sulfide solid electrolytes.

Air stability can be improved by substituting Sn for P, which can form stronger bonds with S. A detailed explanation of this can be provided through the hard and soft acid and base (HSAB) theory.[24,47] Based on the HSAB concept, the weak P–S bond, which causes the poor air stability of Li-argyrodite, is due to the tendency of the hard acid P^{5+} to preferentially bind with the hard base O^{2-} rather than with the soft base S^{2-}. Therefore, substituting a soft acid element like Sn, which can form stronger bonds with S can reduce the reaction with O and improve air stability.[39,48]

The impact of Sn doping on the air stability of the solid electrolyte was investigated as follows. Solid electrolytes were pelletized in a diameter of 10 mm with 150 mg of LPSClBr and Sn5@Agy. These pellets were then exposed to a defined atmosphere at 30 °C for 12 hours. The structural analysis of the air-exposed electrolytes was conducted using XRD, as shown in Fig. 5(b) and (c). XRD revealed the formation of impurity phases in both LPSClBr and Sn5@Agy upon exposure to air. For LPSClBr, numerous unknown impurity peaks (particularly prominent within the 2θ range of 15°–35°) were observed, indicating substantial degradation upon air exposure. In contrast, the Sn5@Agy exhibited minor impurity peaks, suggesting that the formation of secondary phases was effectively suppressed.

The ionic conductivity of electrolytes after air exposure under the specified conditions was also measured. As depicted in Fig. 5(d), the ionic conductivity of the LPSClBr after air exposure fell to 55% (1.01 mS cm^{-1}) of its pre-exposure value (1.81 mS cm^{-1}). However, for Sn5@Agy, the ionic conductivity maintained 67% (1.52 mS cm^{-1}) of its pre-exposure value (2.34 mS cm^{-1}). Consistently, the activation energy of air-exposed Sn5@Agy exhibited a lower value (0.338 eV) compared to LPSClBr (0.350 eV).
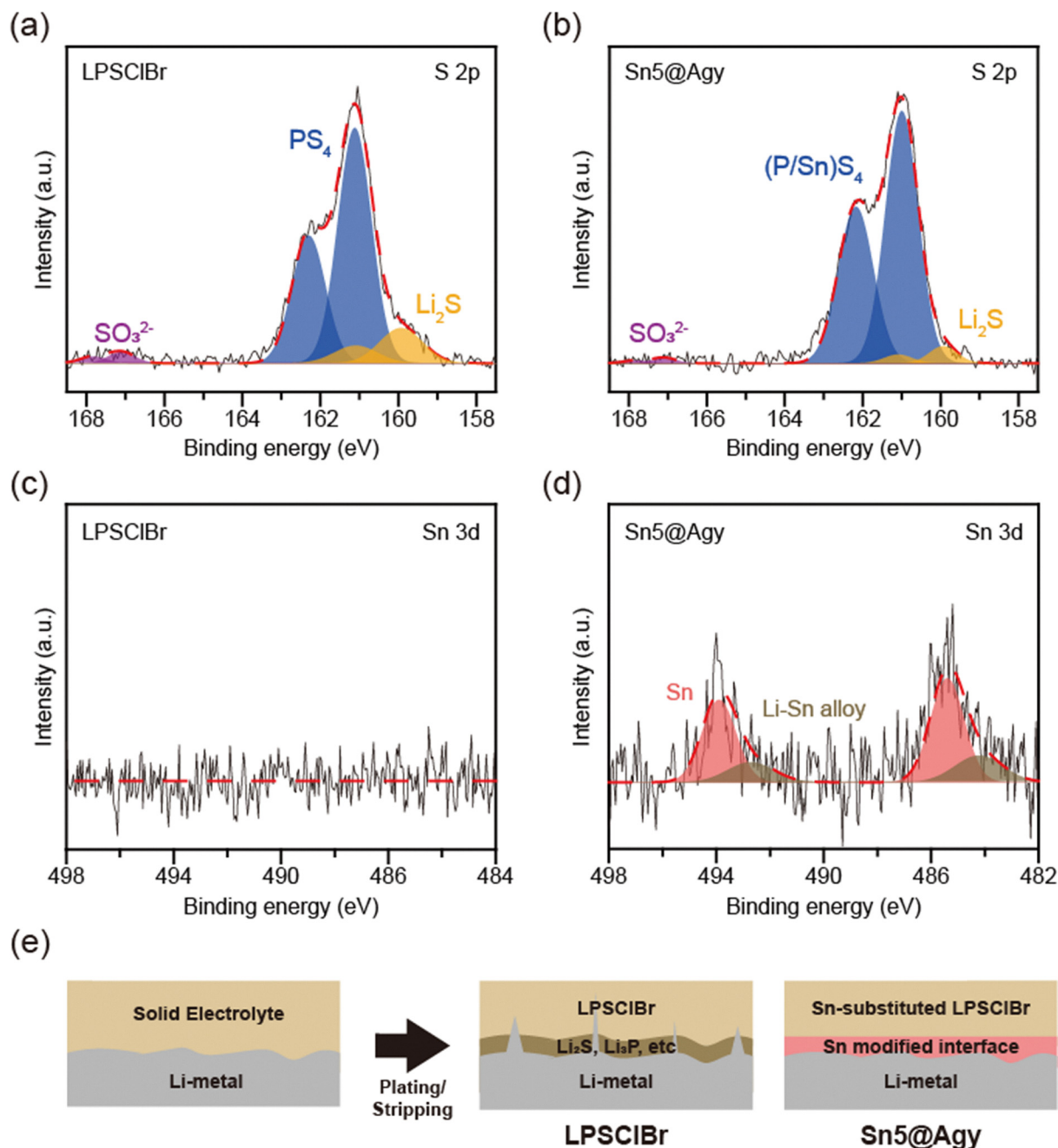
Fig. 4   XPS spectra of the interface between solid electrolyte and lithium metal anode: (a) S 2p spectra of the LPSClBr and Li metal interface after cycling. (b) S 2p spectra of the Sn5@Agy and Li metal interface after cycling. (c) Sn 3d spectra of the LPSClBr and Li metal interface after cycling. (d) Sn 3d spectra of the Sn5@Agy and Li metal interface after cycling. (e) Schematic illustration of improved interfacial stability after Sn substitution.

Furthermore, the effect of Sn substitution on air stability was assessed by measuring the weight change of the electrolyte upon air exposure. As sulfur is replaced by heavier oxygen, the electrolyte undergoes decomposition, as previously described.[24] Fig. 5(e) shows the weight changes of LPSClBr and Sn5@Agy after 6 hours of air exposure. For LPSClBr, the weight increased by 1.97%, whereas for Sn5@Agy exhibited only a 0.65% increase. This observation highlights the enhanced structural and chemical stability achieved by Sn substitution, which significantly reduced electrolyte decomposition. These results demonstrate that the substitution of Sn could enhance the air stability of sulfide solid electrolytes.

3.4. Galvanostatic charge/discharge test for all-solid-state full cells

To evaluate the electrochemical performance of solid electrolytes, ASSBs were assembled using a LiCoO$_2$ cathode and a lithium metal anode as illustrated in Fig. 6(a). The full cells underwent galvanostatic charge–discharge tests within a voltage window of 3.0 to 4.3 V (vs. Li/Li$^+$) at 30 °C. The LPSClBr cell
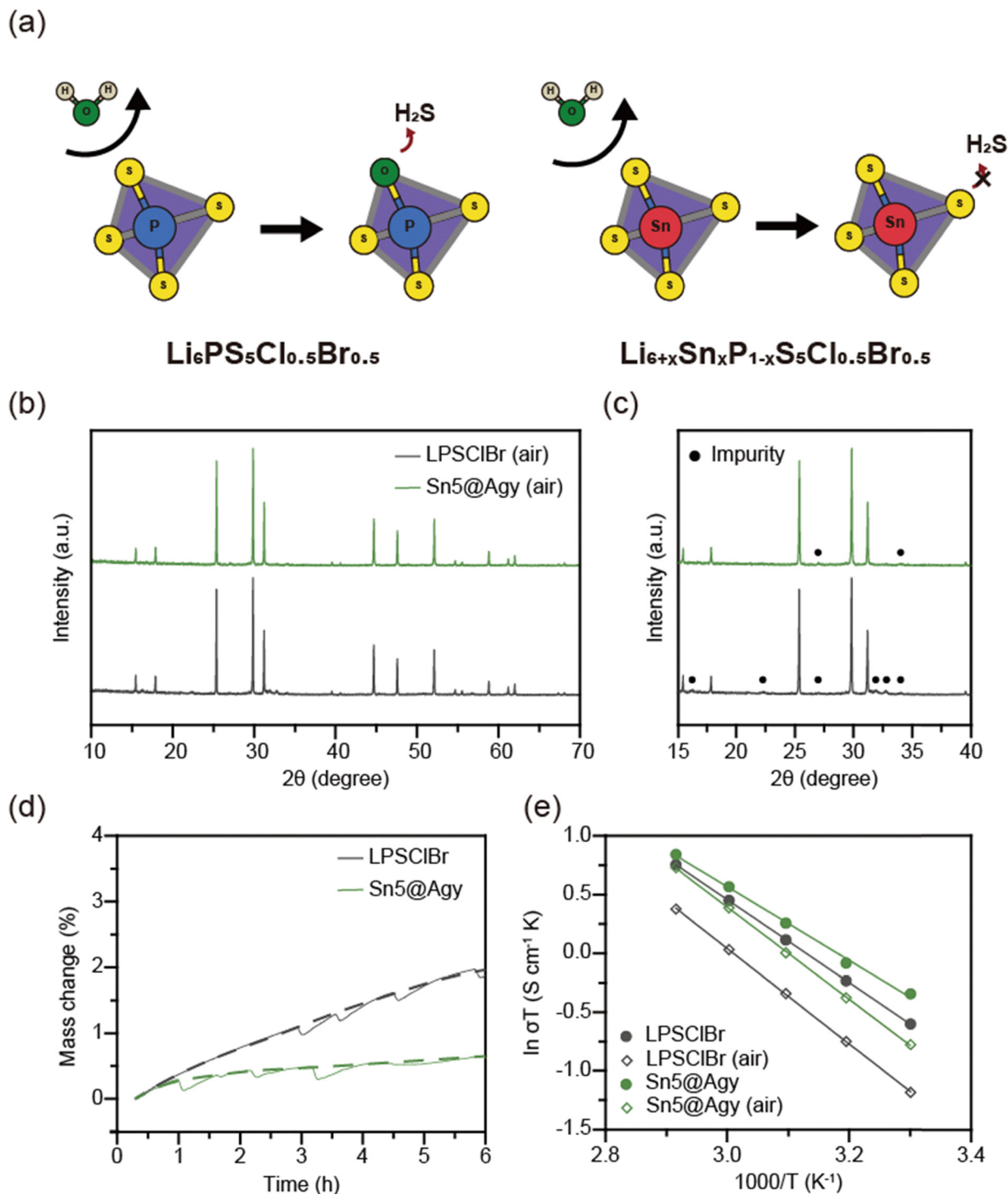
Fig. 5   (a) Schematic diagram of enhanced air stability after Sn substitution. (b) XRD patterns of air exposed $Li_{6+x}Sn_xP_{1-x}S_5Cl_{0.5}Br_{0.5}$ electrolytes (x = 0, 0.05). (c) Magnified XRD patterns of air exposed electrolytes ($15° < \theta < 40°$). (d) Mass change of LPSClBr and Sn5@Agy electrolytes after air exposure. (e) Ionic conductivity change of LPSClBr and Sn5@Agy electrolytes after 12 h of air exposure.

showed an initial specific capacity of 124 mAh g^{-1} and a coulombic efficiency of 70%. In contrast, the Sn5@Agy cell exhibited an improved capacity of 139 mAh g^{-1} and a coulombic efficiency of 80%. The higher coulombic efficiency suggests more reversible lithium-ion intercalation and deintercalation, aligning with the enhanced lithium plating and stripping

processes that reduce lithium source waste.[49,50] Notably, after the 50th cycle, the capacity for LPSClBr was measured at 50.4 mAh g^{-1}, while Sn5@Agy demonstrated a higher capacity of 70.5 mAh g^{-1}. These values represent capacity retention of 40.6% and 50.7%, respectively. After the 50th cycle, the Nyquist plot for the Sn5@Agy cell (Fig. S6(c), ESI†) reveals significantly
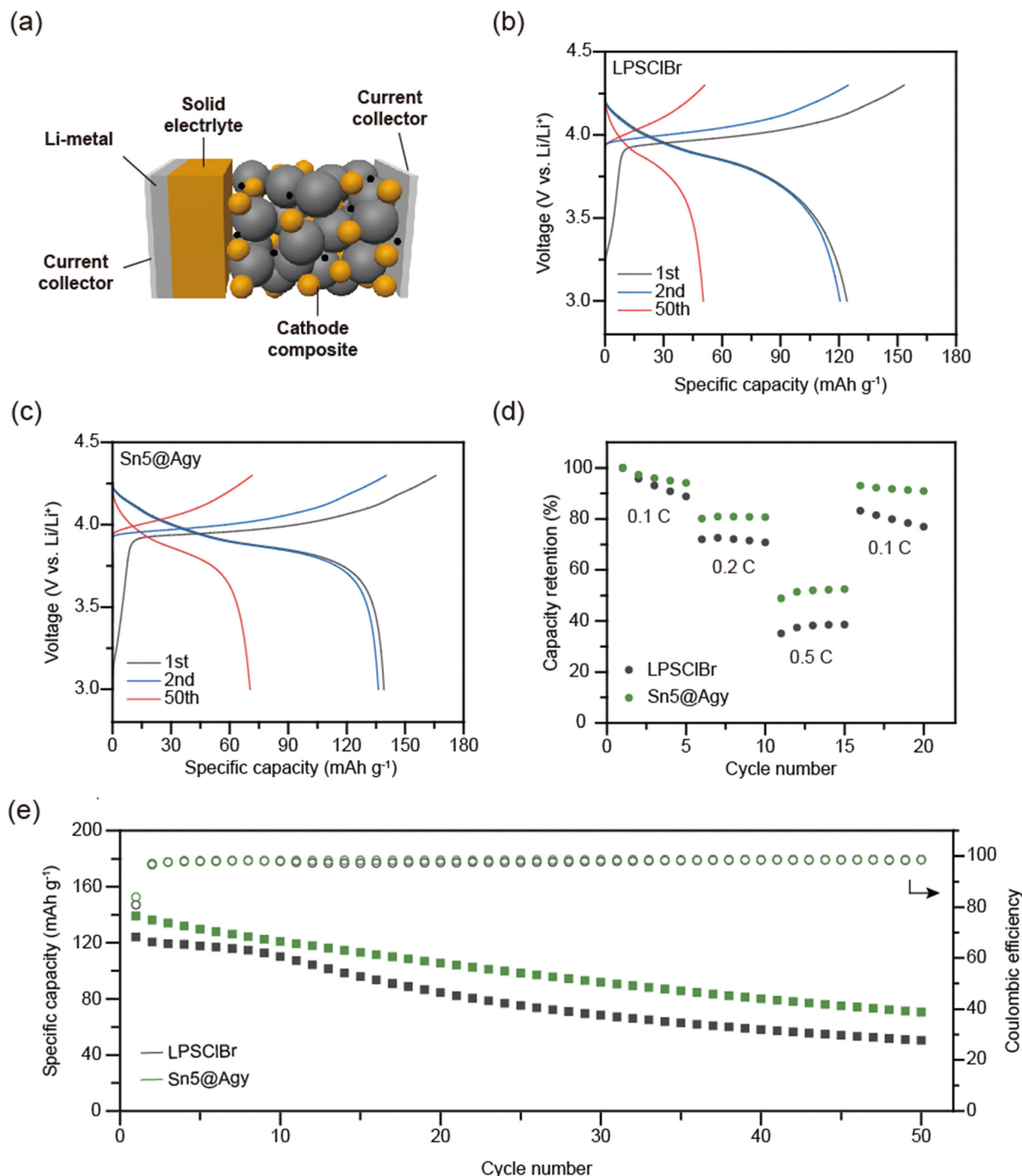
Fig. 6 Galvanostatic charge and discharge test of the full cell: (a) schematic illustration of ASSB. (b) Voltage profile of 1st, 2nd, 50th cycles using LPSClBr electrolyte. (c) Voltage profile of 1st, 2nd, 50th cycles using Sn5@Agy. (d) Rate capability test and capacity retention at various current densities. (e) Cycling performance over 50 cycles at 0.1C.

smaller semicircles compared to the LPSClBr cell (Fig. S6(b), ESI†). This reduction indicates that Sn substitution plays a crucial role in lowering interfacial resistance. The enhanced electrode interfacial stability can be attributed to Sn doping, which helps prevent the formation of insulating interfacial degradation products, thereby improving full cell performance. The rate performance of all-solid-state batteries was evaluated by elevating the current density to 0.1C, 0.2C, and 0.5C, and

then reducing to 0.1C. At a current density of 1C, the specific capacity retention was 35.13% for LPSClBr and 48.87% for Sn5@Agy compared to the first cycle at 0.1C. When the current density is back to 0.1C, the specific capacity recovered to 83.22% for LPSClBr and 93% for Sn5@Agy, indicating superior rate capability after Sn doping. This underscores the improved ionic conductivity and electrochemical stability of the $Li_{6+x}Sn_xP_{1-x}S_5Cl_{0.5}Br_{0.5}$ electrolyte.

4. Conclusion

This study investigated Sn substitution in lithium argyrodite sulfide solid electrolytes as a strategy to enhance their electrochemical and chemical stability. By incorporating halogen elements, the LPSClBr electrolyte was synthesized, exhibiting higher ionic conductivity than LPSBr or LPSI. This approach successfully enabled the substitution of large Sn cations within Cl-containing argyrodite. Our findings confirmed that all Sn-substituted samples preserved the Li-argyrodite structure, with a notable increase in cell volume and Li^+ solubility both of which contributed to improved ionic conductivity. Specifically, the Sn5@Agy sample exhibited the highest ionic conductivity and the lowest activation energy, effectively minimizing impurity formation. Symmetric cell tests demonstrated that Sn substitution enhanced critical current density, enabled stable lithium plating/stripping, and suppressed lithium dendrite growth. XPS analysis further verified the formation of a lithiophilic Li–Sn alloy and a decrease in insulating byproducts such as Li_2S and S–O compounds, leading to improved interfacial stability with the Li metal anode. Under humid conditions, Sn5@Agy also demonstrated superior ionic conductivity retention compared to LPSClBr, as evidenced by EIS measurements. Full cell galvanostatic tests highlighted increased initial discharge capacity and excellent capacity retention over 50 cycles for Sn5@Agy relative to LPSClBr. These improvements, driven by enhanced ionic conductivity and robust interfacial stability against the lithium metal anode, underscore the importance of electrolyte composition modification. The combined effects of halogen incorporation and Sn substitution represent a promising pathway for advancing the performance, stability, and cyclability of lithium argyrodite sulfide-based ASSBs.

Conflicts of interest

There are no conflicts to declare.

Data availability

The data supporting this article have been included as part of the ESI.†

Acknowledgements

References

1 G. Jeong, Y. U. Kim, H. Kim, Y. J. Kim and H. J. Sohn, Prospective materials and applications for Li secondary batteries, *Energy Environ. Sci.*, 2011, **4**, 1986–2002.

2 Y. Ding, Z. P. Cano, A. Yu, J. Lu and Z. Chen, *Electrochem. Energy Rev.*, 2019, **2**, 1–28.

3 M. Li, J. Lu, Z. Chen and K. Amine, 30 Years of Lithium-Ion Batteries, *Adv. Mater.*, 2018, **30**, 1800561.

4 Z. Chang, H. Yang, X. Zhu, P. He and H. Zhou, A stable quasi-solid electrolyte improves the safe operation of highly efficient lithium-metal pouch cells in harsh environments, *Nat. Commun.*, 2022, **13**, 1510.

5 E. Cha, D. K. Kim and W. Choi, Advances of 2D MoS_2 for High-Energy Lithium Metal Batteries, *Front. Energy Res.*, 2021, **9**, 645403.

6 A. Manthiram, X. Yu and S. Wang, Lithium battery chemistries enabled by solid-state electrolytes, *Nat. Rev. Mater.*, 2017, **2**, 16103.

7 Y. K. Sun, Promising All-Solid-State Batteries for Future Electric Vehicles, *ACS Energy Lett.*, 2020, **5**, 3221–3223.

8 T. Schmaltz, F. Hartmann, T. Wicke, L. Weymann, C. Neef and J. Janek, A Roadmap for Solid-State Batteries, *Adv. Energy Mater.*, 2023, **13**, 2301886.

9 D. Lin, Y. Liu and Y. Cui, Reviving the lithium metal anode for high-energy batteries, *Nat. Nanotechnol.*, 2017, **12**, 194–206.

10 C. Wu, J. Lou, J. Zhang, Z. Chen, A. Kakar, B. Emley, Q. Ai, H. Guo, Y. Liang, J. Lou, Y. Yao and Z. Fan, Current status and future directions of all-solid-state batteries with lithium metal anodes, sulfide electrolytes, and layered transition metal oxide cathodes, *Nano Energy*, 2021, **87**, 106081.

11 E. Cha, J. H. Yun, R. Ponraj and D. K. Kim, A mechanistic review of lithiophilic materials: resolving lithium dendrites and advancing lithium metal-based batteries, *Mater. Chem. Front.*, 2021, **5**, 6294–6314.

12 G. Yasin, M. Arif, T. Mehtab, X. Lu, D. Yu, N. Muhammad, M. T. Nazir and H. Song, Understanding and suppression strategies toward stable Li metal anode for safe lithium batteries, *Energy Storage Mater.*, 2020, **25**, 644–678.

13 J. Wu, L. Shen, Z. Zhang, G. Liu, Z. Wang, D. Zhou, H. Wan, X. Xu and X. Yao, All-Solid-State Lithium Batteries with Sulfide Electrolytes and Oxide Cathodes, *Electrochem. Energy Rev.*, 2021, **4**, 101–135.

14 J. Wu, S. Liu, F. Han, X. Yao and C. Wang, Lithium/Sulfide All-Solid-State Batteries using Sulfide Electrolytes, *Adv. Mater.*, 2021, **33**, 2000751.

15 J. C. Bachman, S. Muy, A. Grimaud, H. H. Chang, N. Pour, S. F. Lux, O. Paschos, F. Maglia, S. Lupart, P. Lamp, L. Giordano and Y. Shao Horn, Inorganic Solid-State Electrolytes for Lithium Batteries: Mechanisms and Properties Governing Ion Conduction, *Chem. Rev.*, 2016, **116**, 140–162.

16 C. Yu, L. van Eijck, S. Ganapathy and M. Wagemaker, Synthesis, structure and electrochemical performance of the argyrodite Li_6PS_5Cl solid electrolyte for Li-ion solid state batteries, *Electrochim. Acta*, 2016, **215**, 93–99.

17 S. K. Jung, H. Gwon, S. S. Lee, H. Kim, J. C. Lee, J. G. Chung, S. Y. Park, Y. Aihara and D. Im, Understanding the effects of chemical reactions at the cathode-electrolyte interface in sulfide based all-solid-state batteries, *J. Mater. Chem. A*, 2019, **7**, 22967–22976.

18 J. Shi, P. Li, K. Han, D. Sun, W. Zhao, Z. Liu, G. Liang, K. Davey, Z. Guo and X. Qu, High-rate and durable sulfide-based all-solid-state lithium battery with in situ Li_2O buffering, *Energy Storage Mater.*, 2022, **51**, 306–316.

19 A. Gurung, J. Pokharel, A. Baniya, R. Pathak, K. Chen, B. S. Lamsal, N. Ghimire, W. H. Zhang, Y. Zhou and Q. Qiao, A review on strategies addressing interface incompatibilities in inorganic all-solid-state lithium batteries, *Sustain, Energy Fuels*, 2019, **3**, 3279–3309.

20 Y. Liang, H. Liu, G. Wang, C. Wang, Y. Ni, C. W. Nan and L. Z. Fan, Challenges, interface engineering, and processing strategies toward practical sulfide-based all-solid-state lithium batteries, *InfoMat*, 2022, **4**, e12292.

21 D. H. S. Tan, E. A. Wu, H. Nguyen, Z. Chen, M. A. T. Marple, J. M. Doux, X. Wang, H. Yang, A. Banerjee and Y. S. Meng, Elucidating Reversible Electrochemical Redox of Li_6PS_5Cl Solid Electrolyte, *ACS Energy Lett.*, 2019, **4**, 2418–2427.

22 F. Zhao, S. Zhang, Y. Li and X. Sun, Emerging Characterization Techniques for Electrode Interfaces in Sulfide-Based All-Solid-State Lithium Batteries, *Small Struct.*, 2022, **3**, 2100146.

23 J. Kasemchainan, S. Zekoll, D. Spencer Jolly, Z. Ning, G. O. Hartley, J. Marrow and P. G. Bruce, Critical stripping current leads to dendrite formation on plating in lithium anode solid electrolyte cells, *Nat. Mater.*, 2019, **18**, 1105–1111.

24 P. Lu, D. Wu, L. Chen, H. Li and F. Wu, Air Stability of Solid-State Sulfide Batteries and Electrolytes, *Electrochem. Energy Rev.*, 2022, **5**, 3.

25 Y. T. Chen, M. A. T. Marple, D. H. S. Tan, S. Y. Ham, B. Sayahpour, W.-K. Li, H. Yang, J. B. Lee, H. J. Hah, E. A. Wu, J. M. Doux, J. Jang, P. Ridley, A. Cronk, G. Deysher, Z. Chen and Y. S. Meng, Investigating dry room compatibility of sulfide solid-state electrolytes for scalable manufacturing, *J. Mater. Chem. A*, 2022, **10**, 7155–7164.

26 H. Liu, Q. Zhu, Y. Liang, C. Wang, D. Li, X. Zhao, L. Gao and L. Z. Fan, Versatility of Sb-doping enabling argyrodite electrolyte with superior moisture stability and Li metal compatibility towards practical all-solid-state Li metal batteries, *Chem. Eng. J.*, 2023, **462**, 142183.

27 Z. Jiang, Y. Liu, H. Peng, J. Li, X. Xu, H. Su, Y. Zhong, X. Wang, C. Gu and J. Tu, Enhanced air stability and interfacial compatibility of Li-argyrodite sulfide electrolyte triggered by CuBr co-substitution for all-solid-state lithium batteries, *Energy Storage Mater.*, 2023, **56**, 300–309.

28 S. Ohno, B. Helm, T. Fuchs, G. Dewald, M. A. Kraft, S. P. Culver, A. Senyshyn and W. G. Zeier, Further Evidence for Energy Landscape Flattening in the Superionic Argyrodites $Li_{6+x}P_{1-x}M_xS_5I$ (M = Si, Ge, Sn), *Chem. Mater.*, 2019, **31**, 4936–4944.

29 F. Zhao, J. Liang, C. Yu, Q. Sun, X. Li, K. Adair, C. Wang, Y. Zhao, S. Zhang, W. Li, S. Deng, R. Li, Y. Huang, H. Huang, L. Zhang, S. Zhao, S. Lu and X. Sun, A Versatile Sn-Substituted Argyrodite Sulfide Electrolyte for All-Solid-State Li Metal Batteries, *Adv. Energy Mater.*, 2020, **10**, 1903422.

30 Y. B. Song, D. H. Kim, H. Kwak, D. Han, S. Kang, J. H. Lee, S. M. Bak, K. W. Nam, H. W. Lee and Y. S. Jung, Tailoring Solution-Processable Li Argyrodites $Li_{6+x}P_{1-x}M_xS_5I$ (M = Ge, Sn) and Their Microstructural Evolution Revealed by Cryo-TEM for All-Solid-State Batteries, *Nano Lett.*, 2020, **20**, 4337–4345.

31 D. Wang, H. Shi, S. Wang, X. Wu, W. Jiang, S. Liang and Z. Xu, New insights into Li-argyrodite solid-state electrolytes based on doping strategies, *Coord. Chem. Rev.*, 2024, **508**, 215776.

32 Y. Wang, Y. Wu, Z. Wang, L. Chen, H. Li and F. Wu, Doping strategy and mechanism for oxide and sulfide solid electrolytes with high ionic conductivity, *J. Mater. Chem. A*, 2022, **10**, 4517–4532.

33 B. D. Dandena, D. S. Tsai, S. H. Wu, W. N. Su and B. J. Hwang, Roles of cation-doped Li-argyrodite electrolytes on the efficiency of all-solid-state-lithium batteries, *Energy Storage Mater.*, 2024, **69**, 103305.

34 P. Adeli, J. D. Bazak, K. H. Park, I. Kochetkov, A. Huq, G. R. Goward and L. F. Nazar, Boosting Solid-State Diffusivity and Conductivity in Lithium Superionic Argyrodites by Halide Substitution, *Angew. Chem., Int. Ed.*, 2019, **58**, 8681–8686.

35 M. A. Kraft, S. P. Culver, M. Calderon, F. Böcher, T. Krauskopf, A. Senyshyn, C. Dietrich, A. Zevalkink, J. Janek and W. G. Zeier, Influence of Lattice Polarizability on the Ionic Conductivity in the Lithium Superionic Argyrodites Li_6PS_5X (X = Cl, Br, I), *J. Am. Chem. Soc.*, 2017, **139**, 10909–10918.

36 H. Wang, C. Yu, S. Ganapathy, E. R. H. van Eck, L. van Eijck and M. Wagemaker, A lithium argyrodite $Li_6PS_5Cl_{0.5}Br_{0.5}$ electrolyte with improved bulk and interfacial conductivity, *J. Power Sources*, 2019, **412**, 29–36.

37 R. D. Shannon, Revised Effective Ionic Radii and Systematic Studies of Interatomie Distances in Halides and Chaleogenides, Revised Effective Ionic Radii and Systematic Studies of Interatomie Distances in Halides and Chaleogenides, *Acta Crystallogr., Sect. A*, 1976, **32**, 751–767.

38 S. Wang, Y. Zhang, X. Zhang, T. Liu, Y. H. Lin, Y. Shen, L. Li and C. W. Nan, High-Conductivity Argyrodite Li_6PS_5Cl Solid Electrolytes Prepared via Optimized Sintering Processes for All-Solid-State Lithium-Sulfur Batteries, *ACS Appl. Mater. Interfaces*, 2018, **10**, 42279–42285.

39 K. Kanazawa, S. Yubuchi, C. Hotehama, M. Otoyama, S. Shimono, H. Ishibashi, Y. Kubota, A. Sakuda, A. Hayashi and M. Tatsumisago, Mechanochemical Synthesis and Characterization of Metastable Hexagonal Li_4SnS_4 Solid Electrolyte, *Inorg. Chem.*, 2018, **57**, 9925–9930.

40 K. H. Chen, K. N. Wood, E. Kazyak, W. S. Lepage, A. L. Davis, A. J. Sanchez and N. P. Dasgupta, Dead lithium: Mass transport effects on voltage, capacity, and failure of lithium metal anodes, *J. Mater. Chem. A*, 2017, **5**, 11671–11681.

41 Z. Liu, A. Borodin, G. Li, X. Liu, Y. Li and F. Endres, X-ray Photoelectron Spectroscopy Probing of the Interphase between Solid-State Sulfide Electrolytes and a Lithium Anode, *J. Phys. Chem. C*, 2020, **124**, 300–308.

42 J. Zhang, L. Li, C. Zheng, Y. Xia, Y. Gan, H. Huang, C. Liang, X. He, X. Tao and W. Zhang, Silicon-Doped Argyrodite Solid Electrolyte Li_6PS_5I with Improved Ionic Conductivity and Interfacial Compatibility for High-Performance All-Solid-State Lithium Batteries, *ACS Appl. Mater. Interfaces*, 2020, **12**, 41538–41545.

43 B. deB. Darwent, *Bond Dissociation Energies in Simple Molecules*, 1970.

44 G. Ferraresi, C. Villevieille, I. Czekaj, M. Horisberger, P. Novák and M. El Kazzi, SnO_2 Model Electrode Cycled in Li-Ion Battery Reveals the Formation of Li_2SnO_3 and Li_8SnO_6 Phases through Conversion Reactions, *ACS Appl. Mater. Interfaces*, 2018, **10**, 8712–8720.

45 Y. Ma, L. Wang, S. Fu, R. Luo, W. Qu, X. Hu, R. Chen, F. Wu and L. Li, In situ formation of a Li–Sn alloy protected layer for inducing lateral growth of dendrites, *J. Mater. Chem. A*, 2020, **8**, 23574.

46 Z. Luo, C. Liu, Y. Tian, Y. Zhang, Y. Jiang, J. Hu, H. Hou, G. Zou and X. Ji, Dendrite-free lithium metal anode with lithiophilic interphase from hierarchical frameworks by tuned nucleation, *Energy Storage Mater.*, 2020, **27**, 124–132.

47 L. Du, R. Wu, Z. Wu, H. Huang, Y. Xia, Y. Gan, W. Zhang, X. Xia, X. He and J. Zhang, Research progress of all-solid-state lithium–sulfur batteries with sulfide solid electrolytes: materials, interfaces, challenges, and prospects, *Mater. Chem. Front.*, 2023, **7**, 5760–5785.

48 C. Yu, F. Zhao, J. Luo, L. Zhang and X. Sun, Recent development of lithium argyrodite solid-state electrolytes for solid-state batteries: Synthesis, structure, stability and dynamics, *Nano Energy*, 2021, **83**, 105858.

49 J. Qian, W. A. Henderson, W. Xu, P. Bhattacharya, M. Engelhard, O. Borodin and J. G. Zhang, High rate and stable cycling of lithium metal anode, *Nat. Commun.*, 2015, **6**, 6362.

50 K. K. Fu, Y. Gong, B. Liu, Y. Zhu, S. Xu, Y. Yao, W. Luo, C. Wang, S. D. Lacey, J. Dai, Y. Chen, Y. Mo, E. Wachsman and L. Hu, Toward garnet electrolyte–based Li metal batteries: An ultrathin, highly effective, artificial solid-state electrolyte/metallic Li interface, *Sci. Adv.*, 2017, **3**, e1601659.